Global lakes are warming slower than surface air temperature due to accelerated evaporation

Tong, Yan; Feng, Lian; Wang, Xinchi; Pi, Xuehui; Xu, Wang; Woolway, R. Iestyn

Nature Water

DOI:
10.1038/s44221-023-00148-8

Published: 23/10/2023

Peer reviewed version

Cyswllt i'r cyhoeddiad / Link to publication

Dyfyniad o'r fersiwn a gyhoeddwyd / Citation for published version (APA):
Tong, Y., Feng, L., Wang, X., Pi, X., Xu, W., & Woolway, R. I. (2023). Global lakes are warming slower than surface air temperature due to accelerated evaporation. *Nature Water*, *1*(11), 929-940. https://doi.org/10.1038/s44221-023-00148-8

Hawliau Cyffredinol / General rights
Copyright and moral rights for the publications made accessible in the public portal are retained by the authors and/or other copyright owners and it is a condition of accessing publications that users recognise and abide by the legal requirements associated with these rights.

- Users may download and print one copy of any publication from the public portal for the purpose of private study or research.
- You may not further distribute the material or use it for any profit-making activity or commercial gain
- You may freely distribute the URL identifying the publication in the public portal ?

Take down policy
If you believe that this document breaches copyright please contact us providing details, and we will remove access to the work immediately and investigate your claim.

18. May. 2025

Global lakes are warming slower than surface air temperature due to accelerated evaporation

Authors: Yan Tong[1], Lian Feng[1]*, Xinchi Wang[1], Xuehui Pi[1], Wang Xu[2], R. Iestyn Woolway[3]

Affiliations:

[1] School of Environmental Science and Engineering, Southern University of Science and Technology, Shenzhen, China

[2] Shenzhen Ecological and Environmental Monitoring Center of Guangdong Province, Shenzhen, China

[3] School of Ocean Sciences, Bangor University, Wales

*Correspondence to: fengl@sustech.edu.cn

Abstract: Widespread increases in lake surface water temperature (LSWT) have been documented in recent decades. Yet our understanding of global lake warming is mainly based on summertime measurements and includes relatively few observations from high latitudes (> 60°N) where half of the world's lakes are located. Here, we provide temporally and spatially detailed high-resolution LSWTs for 92,245 lakes (36% are located within the Arctic) based on satellite remote sensing and numerical modeling. The global LSWT data suggested a mean increase of +0.24 °C decade^{-1} (uncertainty = 0.02 °C decade^{-1}) from 1981 to 2020, which is significantly ($P < 0.05$) slower than the change in surface air temperature (SAT, mean rate: +0.29 °C decade^{-1}) during the same period. We show that climatic forces (long-wave radiation, shortwave radiation, and specific humidity) other than SAT contribute more than half of the lake warming, and energy loss through accelerated evaporation rate is mainly responsible for the slower warming rate. Lake warming is likely to continue from 2021 to 2099 unless a low-greenhouse-gas-emission scenario is followed. Our dataset provides important baseline information to further evaluate the physical and biological responses of lakes to past and future warming.

Main

Lakes comprise only 2.2% of the global land surface area, yet they are extremely important natural resources that play a vital role in global hydrological and biological cycles [1,2]. However, lakes are highly vulnerable to climate change [3,4]. One of the most pertinent consequences of climate change in lakes is an increase in lake surface water temperature (LSWT) [5], which can result in a cascade of ecological and environmental impacts. Notably, an increase in LSWT can alter important physical (ice cover, evaporation, stratification, etc.) and biogeochemical (primary production, nutrients, and oxygen concentrations, carbon cycling, etc.) processes in lakes, threatening many key functions of lacustrine ecosystems [4,6-8]. For example, the reduction of dissolved oxygen solubility in warmer waters has resulted in the deoxygenation of many temperate lakes [6]. Warming has also facilitated the increased occurrence of harmful algal blooms [9] and contributed to an increase in reported fish die-off events [10], likewise having a detrimental influence on some of the ecosystem services that lakes provide to society (e.g., drinking water, fisheries, recreation). Unfortunately, under continued global warming, such impacts on lakes are expected to worsen in the future.

Global-scale datasets of LSWT have become increasingly available in recent years, due to the availability of extensive *in situ* and satellite-derived observations [11]. A notable example is the synthesis study of summer months' LSWT for 235 globally distributed lakes by ref. [5], which suggested a higher global average warming rate in lakes (0.34 °C decade^{-1}) compared to surface air temperature (0.25 °C decade^{-1}) between 1985 and 2009 [5]. Rapid lake warming was described as a consequence of, among other things, shorter winter ice cover [12] and changes in cloud cover/incoming solar radiation [13]. However, the global dataset investigated was based solely on summertime observations [5], thus neglecting important changes occurring at other times of the year [14]. More recently, satellite-derived daily observations from thousands of lakes have been compiled into freely-available global datasets (e.g., GloboLakes [15] and ESA CCI Lakes [16]). These data, which are available from 1995 to the near-present, have been used to examine various lake thermal responses to climate change, including surface warming, mixing regimes alterations, and heatwave enhancement [17,18]. However, the comparatively rare coverage of these datasets at high latitudes, and their relatively short temporal coverage, challenge our current understanding of global lake warming. Critically, ~50% of the lakes are located north of 60°N [1], and thus need to be resolved in global scale studies.

An alternative approach for investigating global lake thermal responses to climate change is to analyze simulations from process-based lake models, which have become increasingly available in recent years [19]. Global-scale simulations have been used to investigate historical and future climate change impacts on LSWTs, and to quantify the anthropogenic contribution to lake temperature changes [20,21]. However, current global-scale lake model simulations, such as those provided by the Intersectoral Impact Model Intercomparison Project Lake Sector [19], are typically provided on a gridded basis by assuming invariant lake morphological (i.e., depth, morphology, etc.) and hydrothermal (i.e., heat flux from discharge and sediments) features within a relatively large longitude-latitude grid (e.g., 0.1°, 0.25°) [12,20]. Ultimately, these simulations represent an aggregated "typical lake" for each grid cell. However, as most lakes are smaller than the size of one grid cell, and lake-specific features (e.g., depth) play an important role in their thermal response to climate change [22-24], these global-scale simulations can be considered uncertain [25].

To fill the above knowledge gaps, here we integrate satellite remote sensing and numerical modeling to provide hourly LSWTs for 92,245 lakes, and use them to quantify the warming trends of lakes from 1981 to 2099 at a truly global scale. Our study represents the first comprehensive characterization of changes in global LSWT and the associated surface energy redistribution based on a dataset of high spatiotemporal resolution with extensive global coverage.

The global lake surface water temperature (GLAST) dataset

We established a global lake surface water temperature (GLAST) dataset based on four decades (1981-2020) of Landsat satellite images and a physical model (FLake) [26,27] (see Methods and Extended Data Fig. 1). We initially focused on 1.41 million lakes, polygons for which were provided in the HydroLAKES database [2], while the masks for permanent water, narrow channels (to avoid mixing pixels and land adjacency effects), and limited observations (< 10 cloud-free images over the study period) reduced the number of target lakes to 92,245 (36% are located within the Arctic) (see Methods). The total surface area of these lakes is 2,116,773.2 km^2, representing 72.3% of the global lake area [1]. For each lake, the LSWT was retrieved using Landsat thermal observations from 1981 to 2020, and validated with *in situ* observations when available (see Methods). The long-term satellite-derived LSWT was then used to optimize key parameters of the FLake model, which was used to simulate LSWT for all studied lakes. The climate forcing parameters of the FLake model are air temperature, short- and long-wave radiation, wind speed, and specific humidity [17]. Our extensive global validation efforts showed that the optimized FLake model could accurately simulate LSWT, lake surface energy fluxes, evaporation rate, and ice phenology (Extended Data Fig. 2-3, Supplementary Fig. 1). Furthermore, our simulated LSWTs demonstrate a much greater accuracy compared to the currently available dataset from ERA5-Land (Extended Data Fig. 4). Following the validation of the FLake model, we then performed historical (1981-2020) and future (2021-2099) simulations, with the former simulated hourly and the latter at daily timescales, in line with the temporal resolution of the respective climate forcing datasets (see Methods). We conducted the future simulations under three different anthropogenic greenhouse gas emission scenarios, including the Representative Concentration Pathway (RCP) 2.6 (low-emissions), RCP 6.0 (medium-emissions), and RCP 8.5 (high-emissions) [28].

We selected the simulations over the minimum ice-free period (that is, the intersection of the non-frozen period between 1981 and 2020) for lakes worldwide, examined the long-term LSWT trends, and analyzed the drivers and feedbacks on the distribution of lake surface energy fluxes (see Methods). The average duration of the minimum ice-free period for the lakes studied was 187 ± 125 days. We also performed trend analysis for different seasons, and our four seasons were defined as winter (Months 1-3), spring (4-6), summer (7-9), and autumn (10-12) in the Northern Hemisphere, and summer (1-3), autumn (4-6), winter (7-9), and spring (10-12) in the Southern Hemisphere, following the same practice as in ref. [5]. For the majority of lakes in the southern hemisphere and the middle-to-low latitudes of the northern hemisphere, the minimum ice-free period extends throughout all four seasons of the year (Supplementary Fig. 2). As latitude increases, the minimum ice-free period becomes shorter; for Arctic lakes, 100% of the lakes are covered with ice during winter, and 95.4% and 96.6% are ice-covered during spring and autumn, respectively.

Four decades of global lake warming

The global LSWT dataset showed a mean warming rate of +0.24 °C decade^{-1} (uncertainty = 0.02 °C decade^{-1}) from 1981 to 2020 (Fig. 1). The spatial patterns and warming rates were similar between daytime and nighttime (Supplementary Fig. 3). Of all lakes examined, 41.6% experienced a statistically significant warming trend ($P < 0.05$). Small lakes were warming much faster than large lakes. Notably, the mean warming rate for lakes with a surface area ≤ 1 km^2 was 1.7 times higher than lakes with a surface area > 100 km^2 (Extended Data Fig. 5a). By contrast, cooling trends were observed in only 2.8% of the lakes, mostly in those located in western Siberia, associated with the stratospheric circulation anomaly near the Ural Mountains [29]. A pronounced increase in LSWT was observed in high-latitude regions, with Arctic lakes warming at a rate (+0.48 °C decade^{-1}, uncertainty = 0.03 °C decade^{-1}) twice that of lakes situated south of the Arctic Circle (+0.22 °C decade^{-1}, uncertainty = 0.02 °C decade^{-1}). Such amplified warming of LSWT was comparable to that calculated for surface air temperature (SAT), land surface temperature, and ocean surface temperature in the Arctic regions [30-32].

The global LSWT trend was 17% lower than that calculated for SAT (+0.29 °C decade^{-1}, Fig. 1b), and slower LSWT warming rates were found across all latitudes except for the near-polar regions (Fig. 1c). Matched pair *t-test* also revealed significant ($P < 0.05$) differences between the global trends for LSWT and SAT. As a result, the mean lake-to-air temperature difference has decreased by 0.3 °C (from 1.8 °C to 1.5 °C) over the past four decades (85% of the lakes globally showed higher LSWT than SAT, see Extended Data Fig. 6a-b). By contrast, the lake-air temperature differences have increased at high latitudes (particularly in Northern Europe) due to the greater LSWT warming, highlighting the differential responses of LSWT and SAT to climate change.

Unexpectedly, we found lake warming (+0.64 °C decade^{-1}) and air cooling (-0.17 °C decade^{-1}) in the Arctic during spring. This is the season when Arctic lakes experienced the fastest warming rates, as compared to +0.48 °C decade^{-1} in summer and +0.43 °C decade^{-1} in autumn, respectively (Extended Data Fig. 7). The substantial increase in LSWT in spring was likely due to the prolonged ice-free season during the most recent years and thus an increase in the accumulation of solar radiation at the lake surface [33,34], while the slight decrease in SAT was due to the negative anomalies in the high latitudes of East Asia and western Europe [35]. Moreover, our analysis suggested that the LSWT trend is not only higher in regions with climatologically longer ice duration (i.e., colder regions), but also positively correlates with the loss of ice-cover days (Extended Data Fig. 5b-c). These results also agree with a previous study that suggested lake warming during the months of ice-off was 1.4 times greater than during the open water season [12]. In all other seasons, mean LSWT demonstrated slower increasing rates than SAT in both Arctic and non-Arctic lakes.

Drivers of the global lake warming

We quantified the contributions of key external climate forcing parameters to the global LSWT trends using FLake simulations (Fig. 2, Supplementary Fig. 4). This was accomplished through six groups of simulations, including one reference simulation with the trends of all forcing parameters retained, and five control simulations with the target parameter kept the long-term trend and others were detrended (see Methods). On average, the increase in SAT represents 47% (+0.112 °C decade^{-1}) of lake warming globally. Substantial contributions were identified from long-wave radiation (+0.061 °C decade^{-1}, or 26%) and specific humidity (+0.059 °C decade^{-1}, or 25%). Although solar brightening was also responsible for 7% (+0.017 °C decade^{-1}) of the global lake warming, marked decreases in solar radiation were found in the Canadian and Russian Arctic, the Tibetan Plateau, and India, offsetting of the warming trends (Supplementary Figs. 5g & 6d). By contrast, despite the potential impacts of wind speed on evaporation and stratification [36-38], its contribution to global LSWT trends was minor (-0.005 °C decade^{-1}, -2%). These results corroborate previous findings that other climate variables could considerably influence lake warming besides SAT [13,39-41], whereas the total contribution of the variables to global lake surface warming estimated here (53%) was slightly higher than that by ref. [13,39] (~40%).

Increased evaporation slows down lake warming

Simulations of the lake surface energy fluxes demonstrated that the slower warming of LSWT relative to SAT was primarily due to the energy loss through increased evaporation. From 1981 to 2020, the increasing rate in annual latent heat flux (+1.41 W/m^2 decade^{-1}) was almost three times the increase of incoming net radiation (+0.51 W/m^2 decade^{-1}) (Fig. 3a, c). The rapid increases in latent heat flux can be translated into a mean increase of 7% in the evaporation rate of global lakes during the past four decades, which agrees with previous findings that more energy would be reallocated for evaporation under higher air temperatures [33]. The critical role of evaporation in reducing lake warming is also suggested by the significant negative feedback ($R^2 = 0.58$, $P < 0.05$) between evaporation rate and lake-to-air warming difference for permanently ice-free lakes (Extended Data Fig. 8); such effect of evaporative cooling has also been identified previously in individual lakes [42-45]. This mechanism is also similar to the slower warming rate of the ocean than the land surface, which was attributed primarily to the equilibrium associated with accelerated evaporation over the ocean surface; in contrast, the larger heat capacity of the oceans only represents a transient effect [46]. Meanwhile, the positive sensible heat flux (Fig. 3f) is also responsible for the excessive heat loss from the lake to the air, albeit with a decreasing trend (-0.38 W/m^2 decade^{-1}, Fig. 3e) and a much smaller annual mean value than latent heat flux. Furthermore, heat storage change (ΔG) decreased by 0.52 W/m^2 decade^{-1} over the past four decades (Fig. 3g), indicating a deceleration in both the accumulation of heat storage within lakes and the warming of the lake water column. These changes could have additional implications for the rate of lake stratification and the associated physical and biological processes [47].

The increase in latent heat flux in Arctic lakes during the past four decades (+1.63 W/m^2 decade^{-1}) was higher than in lakes situated elsewhere (+1.39 W/m^2 decade^{-1}), even if the non-Arctic lakes showed approximately twice the value of the annual mean latent heat flux than those in the Arctic (Fig. 3d). Such disproportional increases represented a net evaporation rate increase of 14% in Arctic lakes during the past four decades. To compensate for the excess energy loss of evaporation as well as the substantial decreases in net radiation, ΔG in Arctic lakes demonstrated a mean decreasing rate of -2.12 W/m^2 decade^{-1}, which was four times the global average (-0.52 W/m^2 decade^{-1}).

Future trends and implications of global lake warming

Under a medium-emissions scenario (RCP 6.0), global LSWTs are projected to increase at a rate of +0.30 °C decade^{-1} from 2021 to 2099 (Fig. 4), which is 25% higher than those calculated during the historical period (Fig. 1). Meanwhile, the warming trend would be decelerated in Arctic lakes by -21%. The increase in latent heat flux would be stabilized for global lakes under RCP 6.0, albeit at a rapidly decreased rate (-48%) in Arctic lakes. The sensible heat flux (-0.33 W/m^2 decade^{-1}) and ΔG (-0.25 W/m^2 decade^{-1}) are projected to decrease for global lakes, as the increase of net radiation (+0.78 W/m^2 decade^{-1}) would be insufficient to support the energy loss through latent heat (+1.36 W/m^2 decade^{-1}). The air-to-lake temperature difference is projected to decrease at a slightly slower rate of 0.038 °C decade^{-1} (Extended Data Fig. 6c). Our projection also indicates that the change in LSWT and the energy fluxes under RCP 8.5 will be more pronounced than those seen in the past four decades, especially for Arctic lakes (Supplementary Fig. 7). Nevertheless, negligible future warming in both lakes and air can be expected under a low-emissions scenario (RCP 2.6) (Extended Data Fig. 9).

Our GLAST dataset provides spatially and temporally detailed information on global LSWT changes from 1981 to 2099 (with particularly increased coverage over high latitude regions compared to the existing datasets), providing more comprehensive insights into global lake warming and the associated impacts. For example, our comparison between SAT and LSWT demonstrated significantly slower warming of lakes, which is different from a previous global-scale study where globally indistinguishable trends were found between air and lake temperatures [5]. Our different finding is likely due to the substantial increase in the number of lakes in our study as well as the temporal coverage. Likewise, our increased coverage in cold regions has resulted in a greater projected increase in evaporation rate (27%) by the end of this century compared to Wang et al. (15.7%) [33], while our projections were similar to theirs in tropical and temperate regions (Extended Data Fig. 10). Such detailed mapping of the changes in global lake evaporation rate could help to identify the lake-warming induced increases in drought [48]. In addition, our GLAST dataset can help shed light on the contribution of warming as a major factor driving the observed increase in harmful algal blooms in numerous lakes during recent decades [7-9,49-51].

The responses of lakes to global warming are complex. For example, rising lake temperatures could change not only the solubility and consumption of oxygen and nutrients (the two fundamental processes that sustain lake ecosystems [6,7]), but it could also result in a strengthening of thermal stratification [38]. By limiting the transport of oxygen from surface to bottom waters and the transport of dissolved nutrients in the opposite direction, stratification can lead to further declines in oxygen concentrations, with anoxic conditions at depth having the potential to result in substantial nutrient leakage from the sediments [52], as well as increased production of potent greenhouse gases [53]. Our dataset provides a vital baseline to evaluate the changes in these critical ecological processes and the potential consequences of past and future lake warming.

Methods

Data sources

HydroLAKES. The HydroLAKES database (Version 1.0) provides polygons for 1.4 million lakes and reservoirs worldwide [2], along with various site-specific information, such as lake surface area, mean depth, elevation, etc. These lake-specific attributes are essential for our lake thermodynamic simulations using the FLake model [26,27] (see below). The HydroLAKES dataset was downloaded via https://www.hydrosheds.org/products/hydrolakes.

Global Surface Water (GSW) dataset. We used the 30-m resolution Global Surface Water Occurrence (GSWO) dataset [54] to delineate the extent of our examined global lakes. The GSWO dataset provides the probability of water presence (or water occurrence, ranging from 0 to 100%) for the entire globe over the past four decades, based on millions of historical Landsat satellite images. We also used the monthly history collection of the GSWO dataset to determine the dynamic water masks for lakes with substantial seasonality (see below). The GSW dataset can be freely accessed in Google Earth Engine (GEE) via https://developers.google.com/earth-engine/tutorials/tutorial_global_surface_water_02.

In situ data. Extensive *in situ* datasets were compiled to validate the lake thermal parameters derived from satellites or simulated by model in this study. Specifically, we compiled hourly recorded field measurements of lake temperature sampled near the water surface (depth ≤1 m) through various sources (see Supplementary Table 1) to evaluate the performance of the Landsat-retrieved water surface temperature (see below). A total of 6,755,222 hourly records were obtained, which are distributed at 403 sites worldwide. We also collated observed lake surface heat flux and evaporation rate data, which were available at various temporal resolutions (monthly, seasonal, and annual), from the published literature to validate the model-simulated surface energy budget (Supplementary Table 2). We downloaded *in situ* lake ice phenology records (i.e., the Global Lake and River Ice Phenology Database (GLRIPD, version 1)) from the National Snow and Ice Data Center [55] to validate the model-simulated lake ice freeze-up day, break-up day, and ice duration (see below). The dataset covers approximately 700 lakes in the Northern Hemisphere and is freely available at https://nsidc.org/data/G01377/versions/1.

Landsat satellite data. We used all Collection 1 Tier 1 Landsat 4, 5, 7, and 8 images from 1981-2020 to retrieve global LSWTs. The satellite-derived LSWTs were further used for calibrating the FLake model (see below). The Landsat brightness temperature datasets have spatial resolutions of 120 m, 60 m, and 100 m for Landsat 4/5 Thematic Mapper (TM), Landsat 7 Enhanced Thematic Mapper Plus (ETM+), and Landsat 8 Thermal InfraRed Sensor (TIRS), respectively. The Landsat data are available at https://developers.google.com/earth-engine/datasets/catalog/landsat.

Total Column Water Vapor (TCWV) data. We used the TCWV from NCEP/NCAR Reanalysis data [56] to estimate the atmospheric contribution, which represents a key process in retrieving LSWT using Landsat satellite images. The data is available in GEE at https://developers.google.com/earth-engine/datasets/catalog/NCEP_RE_surface_wv), at a spatial resolution of 2.5° and a temporal resolution of six hours (i.e., four observations provided at 00:00, 06:00, 12:00, and 18:00 UTC each day).

ERA5-Land reanalysis dataset. The European Centre for Medium-Range Weather Forecasts (ECMWF) Re-Analysis v5-Land (ERA5-Land) dataset [57] provides global-land gridded climate forcing data from 1981 to the near present, at hourly temporal resolution and 0.1°×0.1° spatial resolution. Various climate forcing variables of the hourly ERA5-Land dataset were used to calibrate the lake-specific FLake model, including 2-m surface air temperature (SAT, in K), 2-m dew-point temperature (in K), downward surface shortwave radiation (SWdown, in W/m^2), downward surface long-wave radiation (LWdown, W/m^2), surface pressure (Pa), and surface 10-m u and v components of wind (m/s). ERA5-Land provides LSWT data based on grid cells, which were also simulated using the FLake model; however, these simulations were performed by assuming invariant lake morphological (depth, morphology, fetch, etc.) and hydrothermal (heat flux from estuaries and bottom sediments) features within a relatively large grid (i.e., 0.1°). We compared the accuracies of the LSWT between ERA5-Land and our lake-specific simulations (see below). The ERA5-Land dataset can be accessed in GEE at https://developers.google.com/earth-engine/datasets/catalog/ECMWF_ERA5_LAND_HOURLY.

Global ocean surface temperature data. We downloaded the annual anomalies of global ocean surface temperature from 1981 to 2020 to compare with lake surface warming (Fig. 1b). The data was provided by the NOAA National Centers for Environmental Information and available at https://www.ncei.noaa.gov/cag/global/time-series/globe/ocean/ann/3/1981-2020.

The Inter-Sectoral Impact Model Intercomparison Project (ISIMIP2b) dataset. We downloaded future (i.e., 2021-2099) climate-forcing datasets to simulate the future response of lakes to climate change from ISIMIP2b (https://www.isimip.org/) [28]. The datasets include simulations from four bias-corrected climate models (i.e., IPSL-CM5A-LR, GFDL ESM2M, MIROC5, and HadGEM2-ES) under three different greenhouse gas emissions scenarios (RCP 2.6, low emissions; RCP 6.0, moderate-high emissions; RCP 8.5, high emissions), which are provided daily with a spatial resolution of 0.5° [28,58]. The variables we used include air temperature at 2 m, wind speed at 10 m, surface solar, thermal radiation, and specific humidity.

Selection of studied lakes

We used the water occurrence provided by the GSWO dataset to delineate permanent water surfaces within the lake boundaries defined by HydroLAKES, where only pixels with the probability of water presence > 70% were considered permanent water. We further determined the lake center as the point with the largest distance to the shoreline of the permanent water within a lake (D). Note that, when multiple permanent water polygons are available within one lake, we selected the lake center with maximum D. To minimize the potential impacts of mixing pixels [59], land-adjacent effects, and geometric errors [60] on the LSWT retrievals, we only selected lakes with D larger than 3 pixels. For example, we excluded lakes with $D < 300$ m for Landsat 8 TIRS, as the spatial resolution of TIRS is 100 m. We further excluded lakes with insufficient satellite-derived LSWTs (< 10 valid satellite observations over the past four decades) or without climate-forcing data from ERA5-Land (i.e., lakes located near the coast). The final number of lakes selected is 92,245, with 62% located at high latitudes (north of 60°N) and 36% located in the Arctic (north of 66.5°N). The combined area of these lakes is 2,116,773.2 km^2, which accounts for 72.3% of the global lake area. Specifically, the total areas of the studied lakes located north of 60° and in the Arctic region are 437,201.18 km^2 and 140,763.9 km^2, respectively; these areas represent 62% and 54% of the global lake areas at high latitudes and Arctic lakes, respectively. Moreover, the latitudinal distributions of the selected lakes are similar to the patterns of all global lakes, in terms of the lake area and lake number (Supplementary Fig. 8), indicating that the thermal dynamics of global lakes can be well represented using our studied lakes.

Satellite retrieved LSWT dataset

Landsat-retrieved LSWT data from 1981-2020 were used to calibrate lake-specific FLake models (see below). Based on extensive *in situ* data collected worldwide, we validated three widely used LSWT retrieval algorithms, including the generalized single-channel (GSC) algorithm [61-63], the practical single-channel (PSC) algorithm

[64,65], and the statistical mono-window (SMW) algorithm [66,67]. We used the TCWV from the NCEP/NCAR Reanalysis dataset to estimate the atmospheric contribution when performing the satellite retrieval. The satellite-*in situ* match-ups used for the validations were selected via the following criteria: (1) the sampling time difference between *in situ* measurements and satellite overpasses was within 1 h; and (2) no fewer than 50% (that is, 5) of the pixels within the 3 × 3-pixel window centered at the *in situ* stations were valid, and the standard deviation was not higher than 0.5 °C within the window. We considered the satellite LSWT retrieval invalid when (i) the pixel was labeled as high-confidence cloud/cloud shadow or snow/ice or high aerosols or radiometric saturation by the CFMask algorithm [68], (ii) the LSWT retrieval was below 0 °C, or (iii) masked as "land" by the GSW monthly water mask (with auxiliary criteria of MNDWI < 0.05 for "no data"-labeled water mask, where MNDWI = (Green - SWIR)/(Green + SWIR)). A total of 9,948 satellite-*in situ* match-ups were obtained, and the satellite LSWT retrievals were represented by the mean LSWTs of the valid pixels within a 3 × 3-pixel window centered at the *in situ* stations. Our results showed that the SMW algorithm performed best (Supplementary Fig. 9) among the three LSWT retrieval algorithms, with high agreements between the satellite and *in situ* measurements (slope = 0.98, MAE = 0.93 °C, $R^2 = 0.99$). Comparisons of the time-series of satellite retrievals and continuous buoy observations also revealed that the SMW-derived satellite LSWTs could accurately capture the seasonal dynamics in water surface temperature (Supplementary Fig. 10).

Applying the SMW algorithm to global Landsat images over the past four decades, we derived long-term LSWT datasets over global lakes, where the data represent the surface temperature at the time of satellite overpasses (i.e., around 10:00 am local time). For each Landsat observation over a lake, a 3 × 3-pixel kernel around the predefined lake center point was extracted, and the corresponding mean LSWT of the valid pixels within this window was used to represent the LSWT for the lake. We excluded lakes with < 10 Landsat observations, and 91.3% of our finally examined lakes (i.e., 92,245) have at least 100 LSWT satellite retrievals (Supplementary Fig. 11). Such datasets of satellite-derived LSWT "snapshots" allow us to calibrate lake-specific thermodynamic models, which can be used to produce hourly uninterrupted LSWT simulations.

Simulations and validations of LSWTs and heat fluxes

To simulate hourly LSWT and surface heat fluxes, we adopted the one-dimensional thermodynamic lake model FLake [26,27]. The FLake model parameterizes a two-layer water vertical temperature profile, including a vertically homogeneous upper layer (i.e., a mixed layer at the surface) and a lower, stably-stratified layer (i.e., thermally active layer above bottom sediments) [69]. Additional layers are considered when the lake is covered with ice and snow. FLake is capable of simulating temperature profiles and the surface heat flux components in a lake, and the simulations can be performed at hourly to annual scales. The model has been widely used in previous studies to accurately reproduce LSWTs [70,71], lake mixing regimes [18], and ice cover phenologies [18,71-73] at both regional and global scales.

The FLake model requires information on lake-specific characteristics and five climate forcing variables, including SAT, wind speed, short- (solar) wave radiation, long-wave radiation, and specific humidity (estimated directly using dew-point temperature and surface pressure). The long-term climate variables were obtained from the hourly gridded ERA5-Land product (1981-2020), and we extracted the data from the grid cell located at the predetermined lake center. The lake-specific parameters comprise fetch, latitude, lake depth, the light attenuation coefficient (K_d), lake ice albedo (α), and the snow accumulation rate. The lake fetch was fixed as the square root of the lake surface area (provided by the HydroLAKES dataset), and the latitude corresponds to the location of the lake center. However, the other lake-specific parameters for global lakes are either not available or suffer from large uncertainties. Likewise, the wind speed provided by the ERA5-Land dataset is often highly uncertain at the lake surface, as they were based on assimilated data over land instead of lake surfaces [71]. To address this issue, we tuned the lake parameters and wind speed using a total of 2,880 combinations for each lake following a similar method to ref. [71]. We find the optimal set of parameters associated with the minimum median absolute errors (MAE, Supplementary Fig. 12) between the Landsat-retrieved LSWTs and the FLake simulations (i.e., mixed-layer temperature) at the Landsat overpassing time. The selection of trials for the 2,880 combinations was based on previous studies [27,71,74]. For example, the initial lake depth was obtained from the HydroLAKES dataset, which was based on a combination of observations and interpolated DEM [2]. We selected a set of K_d values that represent global ocean waters with varying transparency as referred to ref. [71], and we also provided three additional higher values (up to 3 m^{-1}, a default value widely used for inland lake simulations [27,74]) considering the relatively higher turbidity of many lakes. We set four combinations of snow and ice albedo, as recommended by ref. [71]. Further information on the 2,880 combinations is given in Supplementary Table 3. Note that we also used a perpetual-year solution to determine the initialized prognostic variables (e.g., mixed-layer depth, mixed-layer temperature, mean temperature of the water column) for the FLake model, which is achieved by repeating the forcing data from a representative period (i.e., 1981-1985) and running the FLake model until the simulated annual cycle is stabilized [18]. We examined the calibration performance of the lake-specific FLake models (Supplementary Fig. 12), which showed that the simulated LSWTs agreed well with the satellite retrievals, with a global MAE of 1.2 °C and a median ratio of ~1 (a metric of assessing the extent of over- or under-estimation by comparing the model simulations to Landsat observations). The MAE for deep lakes (water depth > 50 m) was slightly larger than shallower lakes, possibly due to the limitations of the FLake model (2-layer representation of the lake) [69]; while only a small number of lakes have such a depth (~0.7%), and our further validation using *in situ* observations showed high accuracy levels of the globally simulated LSWTs. The satisfactory calibration performance over different types (large/small, deep/shallow, cold/temperate) of lakes could also be revealed by the consistent time-series between satellite retrievals and FLake simulations (Supplementary Fig. 13).

Using the optimized lake-specific FLake models, we simulated the historical (1981-2020) and future (2021-2099) LSWTs and heat fluxes (i.e., net radiation, latent heat flux, sensible heat flux, and heat storage change (ΔG)) for lakes worldwide. The historical simulations were on an hourly basis, which was based on the climate forcing data from the ERA5-Land dataset. In contrast, the future simulations were performed on a daily timescale, using the climate data from four bias-corrected climate models (i.e., IPSL-CM5A-LR, GFDL ESM2M, MIROC5, and HadGEM2-ES) under three different greenhouse gas emissions scenarios (RCP 2.6, RCP 6.0, and RCP 8.5). Under each scenario, we used FLake to perform simulations for each of the four climate models, and the associated mean and standard deviation were estimated (Fig. 4, Extended Data Fig. 9).

We further validated the FLake-simulated LSWT, heat flux, and evaporation rate simulations using extensive independent *in situ* measurements (see Supplementary Tables 1&2). LSWTs were validated at three different temporal scales (hourly, daily, seasonal, and annual). We compared *in situ* LSWT records across 29 lakes and concurrently (time difference < 1 h) simulated LSWT by FLake, which showed good agreement at hourly, daily, seasonal, and annual scales (Extended Data Fig. 2a-d). Consistent temporal changes between FLake simulated LSWTs and independent *in situ* LSWTs over various types of lakes in Supplementary Fig. 14 clearly demonstrated the validity of our simulations. Comparisons with global or regional LSWT products are summarized in Supplementary Table 4. Satisfactory results were also obtained for the net radiation flux, latent heat flux/evaporation rate, sensible heat flux, and heat storage change (Extended Data Fig. 3), which are comparable to or better than other products [33,75,76]. Consistent seasonal dynamics between FLake simulations and *in situ* evaporation rate measurements revealed in Supplementary Fig. 15 could further support the reliability of our simulated evaporation rate data. We also compared the evaporation rate against annual mean data from existing literature (Supplementary Table 5), which also demonstrated good agreements over different lakes. Moreover, the high performance of our lake-specific models can be further verified through their ability to reproduce the lake ice phenologies measured in the GLRIPD dataset (Supplementary Fig. 1). The simulation-based ice phenologies (freeze-up day, break-up day, and duration) were calculated by time-series daily averaged LSWTs (see below), as described in previous studies [19,68,75].

We also compared the accuracy levels of the FLake simulated LSWT with the gridded LSWT product provided by ERA5-Land; ERA5-Land simulations are based on grid cells (0.1° x 0.1°) [76], while our optimized simulations were specifically performed for individual lakes. Our simulations demonstrated substantially reduced uncertainties (MAE decreased by ~1 °C or ~50%) compared to the ERA5-Land LSWT (Extended Data Fig. 4). Such marked improvements highlight the importance of considering lake-specific characteristics with satellite observations as an ideal boundary condition in simulating lake thermodynamics.

We acknowledge that temporal variations in water level can influence lake thermodynamics, including the distribution of incoming solar radiation, heat storage in deeper layers, and temperature profiles within the water column [22,77]. However, incorporating spatial variations in lake depth would introduce further complexity and necessitate a three-dimensional model, which goes beyond the scope of our study. Additionally, obtaining long-term time-series data on lake water levels at a global scale poses a separate challenge. Furthermore, it is important to note that the FLake model we employed in our study does not include water balance processes [74], which prevents the incorporation of water levels when simulating lake thermal dynamics. Despite these limitations, our results are based on the calibration of the lake-specific FLake model using long-term remote sensing observations. This calibration helps to compensate for uncertainties in the simulation of LSWT stemming from various sources (including those associated with lake level dynamics), as demonstrated by the high accuracies of the simulated LSWT and other thermal variables (see above).

It is also worth noting that our optimization process aimed to derive a lake-specific FLake model by optimizing five parameters (i.e., wind speed, lake depth, α, K_d, and the snow accumulation rate). However, these optimized parameters may not necessarily represent the true values for a specific lake. The primary objective of our optimization was to find a set of fixed parameters among the 2,880 combinations that minimize the differences between the simulated LSWTs by FLake and those retrieved by Landsat. However, in reality, some parameters may exhibit significant temporal variations. For instance, K_d in lakes are influenced by the concentrations of chlorophyll and suspended sediments in the water column [78], which can undergo substantial changes over short periods (daily to weekly) due to highly dynamic hydrological and biogeochemical processes within the lake [51,79]. Indeed, to examine the potential impacts of temporal variations in lake parameters on the FLake simulations, we conducted comprehensive validation analyses to assess the performance of our optimized parameter set. The results demonstrated that the optimized FLake model not only achieved high accuracy in simulating LSWTs but also effectively captured lake ice phenology, heat flux, and evaporation rate. Importantly, the model exhibited good performance across different temporal scales, indicating its robustness and ability to capture the dynamics of these variables under varying conditions. These findings further reinforce the reliability and versatility of the FLake model with the optimized parameter set, making it a valuable tool for studying lake thermal dynamics.

Examination of long-term changes

Our analysis of long-term changes in LSWT and heat fluxes only focused on ice-free periods. In this study, we defined the ice-free duration as the period in which the daily mean LSWT is > 1 °C, following the same method as previous studies [18,71,80]. The freeze-up day was determined as the date when the temperature started to drop below 1 °C in the autumn/winter season, while the break-up day was identified as the date when the temperature exceeded 1 °C in the following spring/summer season. The ice-duration period was calculated as the time between these two dates. Our analysis revealed that our lake-specific FLake model effectively reproduces lake ice phenologies, as demonstrated through comparisons with global *in situ* data from the GLRIPD dataset. The slopes between the *in situ* observed and FLake-simulated freeze-up date, break-up date, and ice duration were found to be 0.90, 1.00, and 1.07, respectively. Furthermore, the MAE values for these simulations were 14.0, 6.0, and 13.0 days, respectively (Supplementary Fig. 1). It is important to note that the data from different locations within the GLRIPD dataset may vary in temporal resolution due to its compilation from several individual collections, including records contributed by both citizens and scientists. In general, these matrices indicate comparable levels of accuracy in capturing lake ice phenologies as previous studies [25,81]. We further estimated the changes in ice duration for individual lakes by multiplying the long-term linear regression slope of ice duration by the number of examined years, and used them to explore the potential impacts of ice loss on lake warming (Extended Data Fig. 5c).

For each lake, the above three ice phenologies were computed for multiple years, and the minimum ice-free period (that is, the intersection of the non-frozen period between 1981 and 2020) was considered as our focal time period (i.e., FLake simulations were analyzed only within this period). The minimum ice-free period represents the time span from the latest break-up day to the earliest freeze-up day during the 40-year period. The average duration of the minimum ice-free period for the lakes studied was 187 ± 125 days. For most lakes in the southern hemisphere and the low- and mid-latitudes of the northern hemisphere, the ice-free period extends throughout all four seasons of the year (Supplementary Fig. 2). As latitude increases, the minimum ice-free period becomes shorter; for Arctic lakes, 100% of the lakes are covered with ice during winter, and 95.4% and 96.6% of the lakes remain ice-covered during spring and autumn, respectively.

We calculated the monthly, seasonal, and annual mean LSWT and heat fluxes based on daily simulations within the minimum ice-free period for all examined lakes. To determine the trends of LSWT and heat fluxes, we first estimated their monthly anomalies as the differences from the long-term mean values during 1981-2020, and then estimated the annual mean anomalies across the examined period (1981-2099). We used the linear slope through the annual mean anomalies within a time period (i.e., 1981-2020 or 2021-2099) to represent the trend within the period. We also performed the same trend analysis for different seasons, and our four seasons were defined as winter (Months 1-3), spring (4-6), summer (7-9), and autumn (10-12) in the Northern Hemisphere, and summer (1-3), autumn (4-6), winter (7-9), and spring (10-12) in the Southern Hemisphere, following the same practice as a previous research [5].

We further integrated the global time-series data into 1°×1° grid cells (see Fig. 1a, Fig. 3) and performed the above slope calculations for each grid cell. We adopted a lake area weighted method to estimate the time-series LSWT and heat fluxes within a grid cell (S_{gird}), which can be expressed as

$$S_{grid} = \sum_{i=1}^{m} S_{lake,i}\, A_{lake,i} / \sum_{i=1}^{m} A_{lake,i} \quad (1)$$

where $S_{lake,i}$ and $A_{lake,i}$ are the time-series anomalies and lake surface area for the ith

lake within this grid, respectively, and m is the number of our examined lakes within this grid. Then, the mean trends over global or regional (i.e., Arctic or non-Arctic) scales (S_g) were also estimated using a similar area-weighted scheme, which can be expressed as:

$$S_g = \sum_{j=1}^{n} S_{grid,j}\, A_{grid,j} / \sum_{j=1}^{n} A_{grid,j} \quad (2)$$

where $S_{grid,j}$ and $A_{grid,j}$ are the time-series anomalies and grid area of the jth grid cell within the examined region (i.e., globe, Arctic, or non-Arctic regions), respectively, and n is the number of grid cells within the target region. The daytime/nighttime lake warming trends were calculated using the same method. Daytime and nighttime were defined as the time periods from local 6 am to 6 pm and from local 6 pm to 6 am of the next day, respectively. LSWT trends were also compared with the SATs above the lakes (Fig. 1b). We adopted the same method as LSWT to calculate long-term SAT changes, and only grid cells that cover the studied lakes were included.

We performed the following sensitivity analysis to quantify how could the uncertainty of the daily LSWT simulations propagated into the long-term trends. We first generated random noises with a distribution matching the uncertainty of the daily FLake simulations (median absolute error or MAE = 1.16 °C) (see Supplementary Fig. 16a). These noises were then added to the daily simulated LSWT time series dataset for each lake. Results show that trends between the noise-added and original data are almost the same for all lakes (Supplementary Fig. 16b). We further calculated the standard deviation of these differences across all lakes as the uncertainty propagated by the FLake simulation, and revealed a small uncertainty value (0.02 °C decade^{-1}) relative to the global LSWT trend (0.24 °C decade^{-1}). The uncertainty values were also small when calculated separately for Arctic (0.03 °C decade^{-1}) and non-Arctic lakes (0.02 °C decade^{-1}). Furthermore, considering the limited data availability of Landsat in certain seasons due to cloud cover, we performed optimization of the FLake models by excluding data from one of the four seasons. Our results revealed consistent MAE and trends between the models trained on three seasons and those trained on all four seasons. As such, the impact of reduced data availability in certain seasons on the accuracy of the FLake model is limited.

Attribution of historical lake warming

We quantified the contributions of five individual climate forcing parameters (SAT, wind speed, downward short- and long-wave radiation, and specific humidity) to the historical LSWT trend from 1981 to 2020. The dominant drivers could be determined as the variables with the maximum contributions. In practice, we designed six groups of simulations, with one reference simulation (S1) where all climate parameters changed from 1981 to 2020 (i.e., the same as the above historical simulations), and five control simulations (S2-S6) where one parameter kept the long-term trend and others were detrended by repeating the data in the first year (i.e., 1981) across the four decades. Such a method was similar to those adopted for regional studies [36,40,82], and the detailed parameterizations for the six simulations are listed in Supplementary Table 6. In theory, the LSWT trends from the control simulations are the contributions of the corresponding changed climate parameter to the long-term trend. Indeed, our results showed that the summarized trend (0.244 °C decade^{-1}) from the five control simulations was almost identical to the reference simulation (0.236 °C decade^{-1}) (Fig. 2), further indicating the validity of our attribution analysis.

Impact of lake warming on energy budget

The changes in climate-forcing variables influence various heat exchange processes at the lake-air interface. These processes encompass the absorption of incoming solar radiation (SWdown) and long-wave atmospheric radiation (LWdown), the reflection of solar radiation (SWup), the emission of long-wave lake-surface radiation (LWup), and the exchange of evaporative latent heat and conductive sensible heat [83]. These processes collectively determine the net radiation (Rn, Eq. (3)), which is a fundamental component in the lake surface energy budget [4,84]. The net radiation can be utilized for two heat loss processes: latent heat flux (LE), which serves as the primary energy source for evaporation and is proportional to the evaporation rate [85]; and sensible heat flux (H). Additionally, the net radiation also contributes to heat transfer to deeper layers through heat storage change (ΔG, see Eq. (4)).

$$Rn = SWdown + LWdown - SWup - LWup \quad (3)$$

$$Rn = LE + H + \Delta G \quad (4)$$

We investigated the potential role of increasing evaporation rate on the different warming rates between LSWT and SAT using a climate elasticity model [86]. This model has been extensively employed to quantify the responses of diverse parameters to climate change [87-89], which can be expressed as

$$e = (dLSWT - dSAT)/dLE \quad (5)$$

where the elasticity (e) represents the difference of changes in the lake and air temperature (dLSWT–dSAT) in response to the changes in latent heat flux (dLE).

We utilized the four-decade time series data from 1981 to 2020, focusing on permanently ice-free lakes, to calculate changes in two consecutive years in the respective variables (i.e., dLSWT, dSAT, dLE) for the elasticity calculation. The selection of permanently ice-free lakes is because the energy fluxes of frozen lakes could be modulated substantially by the changes in ice cover over a long-term period [33], complicating the response of the latent heat loss on the different warming rates between lakes and air temperatures. The elasticity (e) was calculated as the linear slope of the scatter plot that includes 39 pairs of matched dLSWT–dSAT and dLE (Extended Data Fig. 8). We found significant negative correlations between the long-term dLSWT – dSAT and dLE ($R^2 = 0.58$, $P < 0.05$), indicating the substantial impacts of evaporation rate increase on the slower rates of LSWT than SAT.

Analyzing the impacts of lake warming on evaporation

To examine the potential historical and future impacts of lake warming on evaporation, we quantified changes in evaporation rate based on the simulated latent heat fluxes (Extended Data Fig. 10). We compared our estimated evaporation rate to that of Wang et al. [33], and the latter includes datasets from both ice-free and ice-covered seasons. The comparisons were conducted using temporally consistent mean annual values for two periods: the past (2006-2015) and the future (2090-2099, representing the end of the 21st century, following a similar practice as previous studies [17,18,33]). The comparisons were performed at both global and regional scales, including tropical, temperate, arid, cold, and polar regions. Global and regional changes were calculated by integrating the differences using a similar lake area-weighted method as in Eq. (2) [90].

Data Availability: The developed GLAST dataset can be accessed through https://zenodo.org/record/8322038.

Code Availability: The source code for the FLake model is opening accessible at http://www.flake.igb-berlin.de/.

Acknowledgements: We thank the USGS for providing global Landsat satellite images, and thank the Google Earth Engine for providing the GSW dataset and global data processing capability. We acknowledge the organizations and individuals (listed in Supplementary Tables 1 & 2) who made substantial efforts to collect global in situ LSWT and surface heat flux datasets. L.F. was supported by the National Natural Science Foundation of China (NOs: 41971304 and 42271322), Guangdong Provincial Higher Education Key Technology Innovation Project (2020ZDZX3006) and by the Support Plan Program of Shenzhen Natural Science Fund under Grant 20200925155151006. We thank four anonymous reviewers for their constructive suggestions and comments in improving our manuscript.

Author Contributions: Y.T.: methodology, data processing and analyses, and writing; L.F.: conceptualization, methodology, funding acquisition, supervision, and writing. X.W. and X.P.: data processing. W.X. and R.I.W. participated in interpreting the results and refining the manuscript.

Competing Interests: The authors declare no competing interests.

Figure Captions:

Fig. 1 | Global patterns of lake warming from 1981 to 2020. (**a**) Global trends in lake surface water temperature (LSWT) from 1981 to 2020. The time-series data used to calculate the LSWT trend are aggregated into 1°×1° grid cells, and a lake area weighted method was adopted to estimate the LSWT time series for each grid (see Methods). Grey indicates regions without examined lakes. The bar charts within the panel show the trends for LSWT and surface air temperature (SAT) for global (G), Arctic (A), and non-Arctic (NA) lakes. (**b**) Comparison of the long-term anomalies (relative to 1981-2020 mean) for global LSWT, ocean surface temperature, and SAT. Their trends over the past decades are annotated. (**c**) Latitudinal profiles of the trends for LSWT and SAT.

Fig. 2 | Attribution of global lake warming over the past four decades. Latitudinal profiles (curves) and globally averaged (bars) contributions to lake warming from five different climate forcing variables, including surface air temperature (SAT), downward surface long-wave radiation (LWdown), specific humidity (SH), downward surface shortwave radiation (SWdown), and surface wind speed (U). The numbers outside and within (if applicable) the parentheses are the absolute (°C decade^{-1}) and relative contributions (%) to global lake warming for each variable. The grey bar (labeled as "sum") and grey curve indicate the sum of individual contributions of each variable, and the black bar (labeled as "reference") and black curve show the results of the reference simulation (see Methods). The reference simulation represents the FLake simulation with the trends of all forcing variables retained. The contributions of five variables were estimated through control simulations where the target variable kept the long-term trend and others were detrended.

Fig. 3 | Global patterns of lake surface heat fluxes and their trends. Left panels: long-term trends from 1981 to 2020 (in W/m^2 decade^{-1}). Right panels: climatological annual mean values (in W/m^2). (**a, b**) Rn: net radiation flux, (**c, d**) LE: latent heat flux, (**e, f**) H: sensible heat flux, and (**g, h**) ΔG: heat storage change. The bar chart within each panel demonstrates the average values for global (G), Arctic (A), and non-Arctic (NA) lakes.

Fig. 4 | Long-term changes in LSWT, SAT, and heat fluxes from 1981 to 2099. (a) LSWT, **(b)** SAT, **(c)** Net radiation flux (Rn), **(d)** Latent heat flux (LE), (**e**) Sensible heat flux (H), and (**f**) Heat storage change (ΔG). The data are presented as the anomalies relative to 1981-2020 mean, with the results for global, Arctic, and non-Arctic lakes shown separately. Future (2021-2099) conditions were simulated under a high emissions scenario (RCP 6.0). Other RCP scenarios are shown in Extended Data Fig. 9. The linear slopes (units: °C decade^{-1} in **a**-**b**, W/m^2 decade^{-1} in **c**-**f**) for historical (1981-2020) and future (2021-2099) periods are annotated (the font colors correspond to the respective curves), and statistically significant trends are indicated by "*". The shadings associated with the future data represent the standard deviations across the four climate model projections.

References

1. Pi, X. *et al.* Mapping global lake dynamics reveals the emerging roles of small lakes. *Nature Communications* **13**, 1-12 (2022).

2 Messager, M. L., Lehner, B., Grill, G., Nedeva, I. & Schmitt, O. Estimating the volume and age of water stored in global lakes using a geo-statistical approach. *Nature Communications* **7**, 1-11 (2016).

3 Adrian, R. *et al.* Lakes as sentinels of climate change. *Limnology and oceanography* **54**, 2283-2297 (2009).

4 Woolway, R. I. *et al.* Global lake responses to climate change. *Nature Reviews Earth & Environment* **1**, 388-403 (2020).

5 O'Reilly, C. M. *et al.* Rapid and highly variable warming of lake surface waters around the globe. *Geophysical Research Letters* **42**, 10,773-710,781 (2015).

6 Jane, S. F. *et al.* Widespread deoxygenation of temperate lakes. *Nature* **594**, 66-70 (2021).

7 Winder, M. Lake warming mimics fertilization. *Nature Climate Change* **2**, 771-772 (2012).

8 Paerl, H. W. & Huisman, J. Blooms like it hot. *Science* **320**, 57-58 (2008).

9 Posch, T., Köster, O., Salcher, M. M. & Pernthaler, J. Harmful filamentous cyanobacteria favoured by reduced water turnover with lake warming. *Nature Climate Change* **2**, 809-813 (2012).

10 Till, A., Rypel, A. L., Bray, A. & Fey, S. B. Fish die-offs are concurrent with thermal extremes in north temperate lakes. *Nature Climate Change* **9**, 637-641 (2019).

11 Sharma, S. *et al.* A global database of lake surface temperatures collected by in situ and satellite methods from 1985–2009. *Scientific data* **2**, 1-19 (2015).

12 Li, X., Peng, S., Xi, Y., Woolway, R. I. & Liu, G. Earlier ice loss accelerates lake warming in the Northern Hemisphere. *Nature Communications* **13**, 1-9 (2022).

13 Schmid, M. & Köster, O. Excess warming of a Central European lake driven by solar brightening. *Water Resources Research* **52**, 8103-8116 (2016).

14 Winslow, L. A., Read, J. S., Hansen, G. J., Rose, K. C. & Robertson, D. M. Seasonality of change: Summer warming rates do not fully represent effects of climate change on lake temperatures. *Limnology and Oceanography* **62**, 2168-2178 (2017).

15 Carrea, L. & Merchant, C. GloboLakes: Lake Surface Water Temperature (LSWT) version 4.0 (1995-2016). *Centre for Environmental Data Analysis* (2019).

16 Carrea, L. C., J.-F.; Liu, X.; Wu, Y.; Bergé-Nguyen, M.; Calmettes, B.; Duguay, C.; Jiang, D.; Merchant, C.J.; Mueller, D.; Selmes, N.; Simis, S.; Spyrakos, E.; Stelzer, K.; Warren, M.; Yesou, H.; Zhang, D. . ESA Lakes Climate Change Initiative (Lakes_cci): Lake products, Version 2.0.2. NERC EDS Centre for Environmental Data Analysis, 06 July 2022. doi:10.5285/a07deacaffb8453e93d57ee214676304. http://dx.doi.org/10.5285/a07deacaffb8453e93d57ee214676304. (2022).

17 Woolway, R. I. *et al.* Lake heatwaves under climate change. *Nature* **589**, 402-407 (2021).

18 Woolway, R. I. & Merchant, C. J. Worldwide alteration of lake mixing regimes in response to climate change. *Nature Geoscience* **12**, 271-276 (2019).

19 Golub, M. *et al.* A framework for ensemble modelling of climate change impacts on lakes worldwide: the ISIMIP Lake Sector. *Geoscientific Model Development* **15**, 4597-4623 (2022).

20 Grant, L. *et al.* Attribution of global lake systems change to anthropogenic forcing. *Nature Geoscience* **14**, 849-854 (2021).

21 Woolway, R. I., Albergel, C., Frölicher, T. L. & Perroud, M. Severe Lake Heatwaves Attributable to Human-Induced Global Warming. *Geophysical Research Letters* **49**, e2021GL097031 (2022).

22 Kraemer, B. M. *et al.* Morphometry and average temperature affect lake stratification responses to climate change. *Geophysical Research Letters* **42**, 4981-4988 (2015).

23 Toffolon, M. *et al.* Prediction of surface temperature in lakes with different morphology using air temperature. *Limnology and Oceanography* **59**, 2185-2202 (2014).

24 Woolway, R. I. & Merchant, C. J. Amplified surface temperature response of cold, deep lakes to inter-annual air temperature variability. *Scientific Reports* **7**, 1-8 (2017).

25 Wang, X. *et al.* Continuous loss of global lake ice across two centuries revealed by satellite observations and numerical modeling. *Geophysical Research Letters* **49**, e2022GL099022 (2022).

26 Mironov, D. V. *Parameterization of lakes in numerical weather prediction: Description of a lake model*. (DWD Offenbach, Germany, 2008).

27 Mironov, D. *et al.* Implementation of the lake parameterisation scheme FLake into the numerical weather prediction model COSMO. (2010).

28 Frieler, K. *et al.* Assessing the impacts of 1.5 C global warming–simulation protocol of the Inter-Sectoral Impact Model Intercomparison Project (ISIMIP2b). *Geoscientific Model Development* **10**, 4321-4345 (2017).

29 Zhang, P. *et al.* A stratospheric pathway linking a colder Siberia to Barents-Kara Sea sea ice loss. *Science Advances* **4**, eaat6025, doi:10.1126/sciadv.aat6025.

30 Screen, J. A. & Simmonds, I. The central role of diminishing sea ice in recent Arctic temperature amplification. *Nature* **464**, 1334-1337 (2010).

31 Shu, Q. *et al.* Arctic Ocean Amplification in a warming climate in CMIP6 models. *Science Advances* **8**, eabn9755 (2022).

32 Wang, Y.-R., Hessen, D. O., Samset, B. H. & Stordal, F. Evaluating global and regional land warming trends in the past decades with both MODIS and ERA5-Land land surface temperature data. *Remote Sensing of Environment* **280**, 113181 (2022).

33 Wang, W. *et al.* Global lake evaporation accelerated by changes in surface energy allocation in a warmer climate. *Nature Geoscience* **11**, 410-414 (2018).

34 Zhong, Y., Notaro, M., Vavrus, S. J. & Foster, M. J. Recent accelerated warming of the Laurentian Great Lakes: Physical drivers. *Limnology and Oceanography* **61**, 1762-1786 (2016).

35 Zhang, X., Wu, B. & Ding, S. Influence of spring Arctic sea ice melt on Eurasian surface air temperature. *Climate Dynamics*, doi:10.1007/s00382-022-06267-4 (2022).

36 Woolway, R. I. *et al.* Northern hemisphere atmospheric stilling accelerates lake thermal responses to a warming world. *Geophysical Research Letters* **46**, 11983-11992 (2019).

37 Austin, J. A. & Colman, S. M. Lake Superior summer water temperatures are increasing more rapidly than regional air temperatures: A positive ice-albedo feedback. *Geophysical Research Letters* **34** (2007).

38 Boehrer, B. & Schultze, M. Stratification of lakes. *Reviews of Geophysics* **46**

(2008).

39 Schmid, M., Hunziker, S. & Wüest, A. Lake surface temperatures in a changing climate: a global sensitivity analysis. *Climatic change* **124**, 301-315 (2014).

40 Li, X., Peng, S., Deng, X., Su, M. & Zeng, H. Attribution of lake warming in four shallow lakes in the middle and lower Yangtze River Basin. *Environmental Science & Technology* **53**, 12548-12555 (2019).

41 Shi, Y. *et al.* Drivers of warming in Lake Nam Co on Tibetan Plateau over the past 40 years. *Journal of Geophysical Research: Atmospheres* **127**, e2021JD036320 (2022).

42 Hondzo, M. & Stefan, H. G. Regional water temperature characteristics of lakes subjected to climate change. *Climatic change* **24**, 187-211 (1993).

43 Mohseni, O. & Stefan, H. G. Stream temperature/air temperature relationship: a physical interpretation. *Journal of Hydrology* **218**, 128-141 (1999).

44 Peeters, F., Livingstone, D. M., Goudsmit, G.-H., Kipfer, R. & Forster, R. Modeling 50 years of historical temperature profiles in a large central European lake. *Limnology and Oceanography* **47**, 186-197 (2002).

45 Lenters, J. D., Kratz, T. K. & Bowser, C. J. Effects of climate variability on lake evaporation: Results from a long-term energy budget study of Sparkling Lake, northern Wisconsin (USA). *Journal of Hydrology* **308**, 168-195 (2005).

46 Sutton, R. T., Dong, B. & Gregory, J. M. Land/sea warming ratio in response to climate change: IPCC AR4 model results and comparison with observations. *Geophysical research letters* **34** (2007).

47 Ladwig, R. *et al.* Lake thermal structure drives interannual variability in summer anoxia dynamics in a eutrophic lake over 37 years. *Hydrology and Earth System Sciences* **25**, 1009-1032 (2021).

48 Cook, B. I. *et al.* Megadroughts in the common Era and the anthropocene. *Nature Reviews Earth & Environment*, 1-17 (2022).

49 Hou, X. *et al.* Global mapping reveals increase in lacustrine algal blooms over the past decade. *Nature Geoscience* **15**, 130-134 (2022).

50 Beaulieu, M., Pick, F. & Gregory-Eaves, I. Nutrients and water temperature are significant predictors of cyanobacterial biomass in a 1147 lakes data set. *Limnology and Oceanography* **58**, 1736-1746 (2013).

51 Yindong, T. *et al.* Lake warming intensifies the seasonal pattern of internal nutrient cycling in the eutrophic lake and potential impacts on algal blooms. *Water Research* **188**, 116570 (2021).

52 North, R. P., North, R. L., Livingstone, D. M., Köster, O. & Kipfer, R. Long-term changes in hypoxia and soluble reactive phosphorus in the hypolimnion of a large temperate lake: consequences of a climate regime shift. *Global change Biology* **20**, 811-823 (2014).

53 Davidson, T. A. *et al.* Synergy between nutrients and warming enhances methane ebullition from experimental lakes. *Nature Climate Change* **8**, 156-160 (2018).

54 Pekel, J.-F., Cottam, A., Gorelick, N. & Belward, A. S. High-resolution mapping of global surface water and its long-term changes. *Nature* **540**, 418-422 (2016).

55 Benson, B. & Magnuson, J. Global lake and river ice phenology database. *Digital Media* (2000).

56 Kalnay, E. *et al.* The NCEP/NCAR 40-year reanalysis project. *Bulletin of the American Meteorological Society* **77**, 437-472 (1996).

57 Muñoz Sabater, J. ERA5-Land hourly data from 1981 to present. *Copernicus Climate Change Service (C3S) Climate Data Store (CDS)* **10** (2019).

58 Van Vuuren, D. P. *et al.* The representative concentration pathways: an overview. *Climatic Change* **109**, 5-31 (2011).

59 Attiah, G., Kheyrollah Pour, H. & Scott, K. A. Lake surface temperature retrieved from Landsat satellite series (1984 to 2021) for the North Slave Region. *Earth System Science Data* **15**, 1329-1355 (2023).

60 Kardoulas, N., Bird, A. & Lawan, A. Geometric correction of SPOT and Landsat imagery: a comparison of map-and GPS-derived control points. *Photogrammetric Engineering and Remote Sensing* **62**, 1173-1177 (1996).

61 Jiménez‐Muñoz, J. C. & Sobrino, J. A. A generalized single‐channel method for retrieving land surface temperature from remote sensing data. *Journal of geophysical research: atmospheres* **108** (2003).

62 Jiménez-Muñoz, J. C. *et al.* Revision of the single-channel algorithm for land surface temperature retrieval from Landsat thermal-infrared data. *IEEE Transactions on geoscience and remote sensing* **47**, 339-349 (2008).

63 Jiménez-Muñoz, J. C., Sobrino, J. A., Skoković, D., Mattar, C. & Cristobal, J. Land surface temperature retrieval methods from Landsat-8 thermal infrared sensor data. *IEEE Geoscience and remote sensing letters* **11**, 1840-1843 (2014).

64 Wang, M. *et al.* An efficient framework for producing Landsat-based land surface temperature data using Google Earth engine. *IEEE Journal of Selected Topics in Applied Earth Observations and Remote Sensing* **13**, 4689-4701 (2020).

65 Wang, M., Zhang, Z., Hu, T. & Liu, X. A practical single‐channel algorithm for land surface temperature retrieval: application to landsat series data. *Journal of Geophysical Research: Atmospheres* **124**, 299-316 (2019).

66 Ermida, S. L., Soares, P., Mantas, V., Göttsche, F.-M. & Trigo, I. F. Google earth engine open-source code for land surface temperature estimation from the landsat series. *Remote Sensing* **12**, 1471 (2020).

67 Duguay-Tetzlaff, A. *et al.* Meteosat land surface temperature climate data record: Achievable accuracy and potential uncertainties. *Remote Sensing* **7**, 13139-13156 (2015).

68 Foga, S. *et al.* Cloud detection algorithm comparison and validation for operational Landsat data products. *Remote Sensing of Environment* **194**, 379-390 (2017).

69 Kirillin, G. Modeling the impact of global warming on water temperature and seasonal mixing regimes in small temperate lakes. (2010).

70 Su, D. *et al.* Numerical study on the response of the largest lake in China to climate change. *Hydrology and Earth System Sciences* **23**, 2093-2109 (2019).

71 Layden, A., MacCallum, S. N. & Merchant, C. J. Determining lake surface

water temperatures worldwide using a tuned one-dimensional lake model (FLake, v1). *Geoscientific Model Development* **9**, 2167-2189 (2016).

72 Kheyrollah Pour, H., Duguay, C., Martynov, A. & Brown, L. Simulation of surface temperature and ice cover of large northern lakes with 1-D models: a comparison with MODIS satellite data and in situ measurements. *Tellus A: Dynamic Meteorology and Oceanography* **64**, 17614 (2012).

73 Salgado, R. & Le Moigne, P. Coupling of the FLake model to the Surfex externalized surface model. (2010).

74 Balsamo, G. *et al.* On the contribution of lakes in predicting near-surface temperature in a global weather forecasting model. *Tellus A: Dynamic Meteorology and Oceanography* **64**, 15829 (2012).

75 Martens, B. *et al.* Evaluating the land-surface energy partitioning in ERA5. *Geoscientific Model Development* **13**, 4159-4181 (2020).

76 Muñoz-Sabater, J. *et al.* ERA5-Land: A state-of-the-art global reanalysis dataset for land applications. *Earth System Science Data* **13**, 4349-4383 (2021).

77 Kerimoglu, O. & Rinke, K. Stratification dynamics in a shallow reservoir under different hydro‐meteorological scenarios and operational strategies. *Water Resources Research* **49**, 7518-7527 (2013).

78 Heiskanen, J. J. *et al.* Effects of water clarity on lake stratification and lake‐atmosphere heat exchange. *Journal of Geophysical Research: Atmospheres* **120**, 7412-7428 (2015).

79 Huang, C. *et al.* Wind and rainfall regulation of the diffuse attenuation coefficient in large, shallow lakes from long‐term MODIS observations using a semianalytical model. *Journal of Geophysical Research: Atmospheres* **122**, 6748-6763 (2017).

80 Layden, A., Merchant, C. & MacCallum, S. Global climatology of surface water temperatures of large lakes by remote sensing. *International Journal of Climatology* **35**, 4464-4479 (2015).

81 Zhao, G., Li, Y., Zhou, L. & Gao, H. Evaporative water loss of 1.42 million global lakes. *Nature communications* **13**, 1-10 (2022).

82 Schmid, M. & Köster, O. Excess warming of a C entral E uropean lake driven by solar brightening. *Water Resources Research* **52**, 8103-8116 (2016).

83 Edinger, J. E., Duttweiler, D. W. & Geyer, J. C. The response of water temperatures to meteorological conditions. *Water Resources Research* **4**, 1137-1143 (1968).

84 Livingstone, D. M. Impact of secular climate change on the thermal structure of a large temperate central European lake. *Climatic change* **57**, 205-225 (2003).

85 Gianniou, S. K. & Antonopoulos, V. Z. Evaporation and energy budget in Lake Vegoritis, Greece. *Journal of Hydrology* **345**, 212-223 (2007).

86 Sankarasubramanian, A., Vogel, R. M. & Limbrunner, J. F. Climate elasticity of streamflow in the United States. *Water Resources Research* **37**, 1771-1781 (2001).

87 Wagener, T., Reinecke, R. & Pianosi, F. On the evaluation of climate change impact models. *Wiley Interdisciplinary Reviews: Climate Change* **13**, e772

(2022).

88 Li, D. *et al.* Exceptional increases in fluvial sediment fluxes in a warmer and wetter High Mountain Asia. *Science* **374**, 599-603 (2021).

89 Liu, Z., Han, J. & Yang, H. Assessing the ability of potential evaporation models to capture the sensitivity to temperature. *Agricultural and forest meteorology* **317**, 108886 (2022).

90 Peel, M. C., Finlayson, B. L. & McMahon, T. A. Updated world map of the Köppen-Geiger climate classification. *Hydrology and earth system sciences* **11**, 1633-1644 (2007).

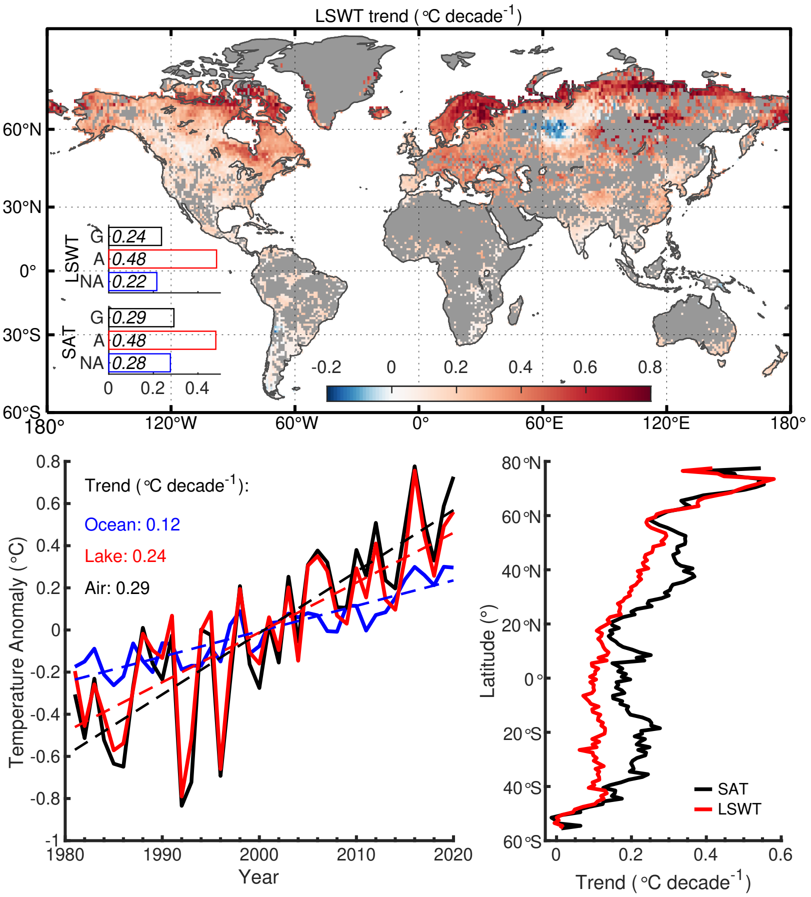
LSWT trend (℃ decade^{-1})
60°N
30°N
0°
30°S
60°S
180°
120°W
60°W
0°
60°E
120°E
180°
LSWT
G 0.24
A 0.48
NA 0.22
SAT
G 0.29
A 0.48
NA 0.28
0
0.2
0.4
-0.2
0
0.2
0.4
0.6
0.8
Trend (℃ decade^{-1}):
Ocean: 0.12
Lake: 0.24
Air: 0.29
Temperature Anomaly (℃)
0.8
0.6
0.4
0.2
0
-0.2
-0.4
-0.6
-0.8
-1
1980
1990
2000
2010
2020
Year
80°N
60°N
40°N
20°N
0°
20°S
40°S
60°S
Latitude (°)
SAT
LSWT
0
0.2
0.4
0.6
Trend (℃ decade^{-1})

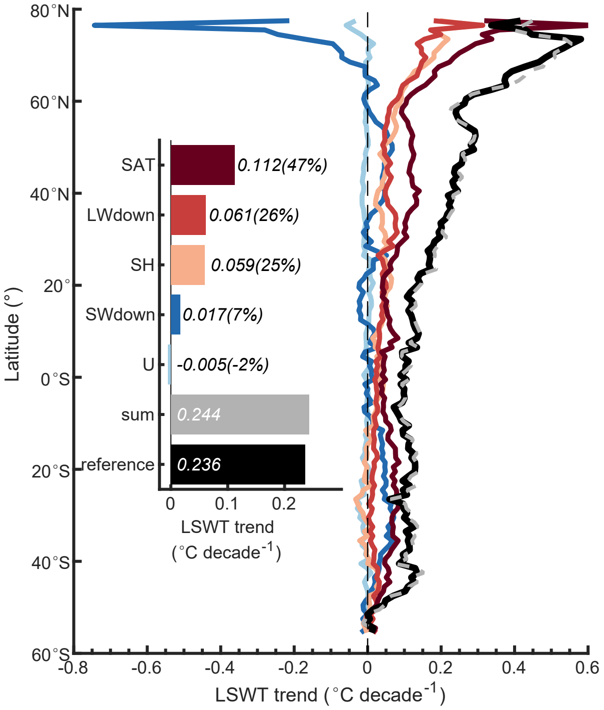
80°N
60°N
40°N
20°
0°S
20°S
40°S
60°S
Latitude (°)
-0.8
-0.6
-0.4
-0.2
0
0.2
0.4
0.6
LSWT trend (°C decade^{-1})
SAT
LWdown
SH
SWdown
U
sum
reference
0.112(47%)
0.061(26%)
0.059(25%)
0.017(7%)
-0.005(-2%)
0.244
0.236
0
0.1
0.2
LSWT trend
(°C decade^{-1})

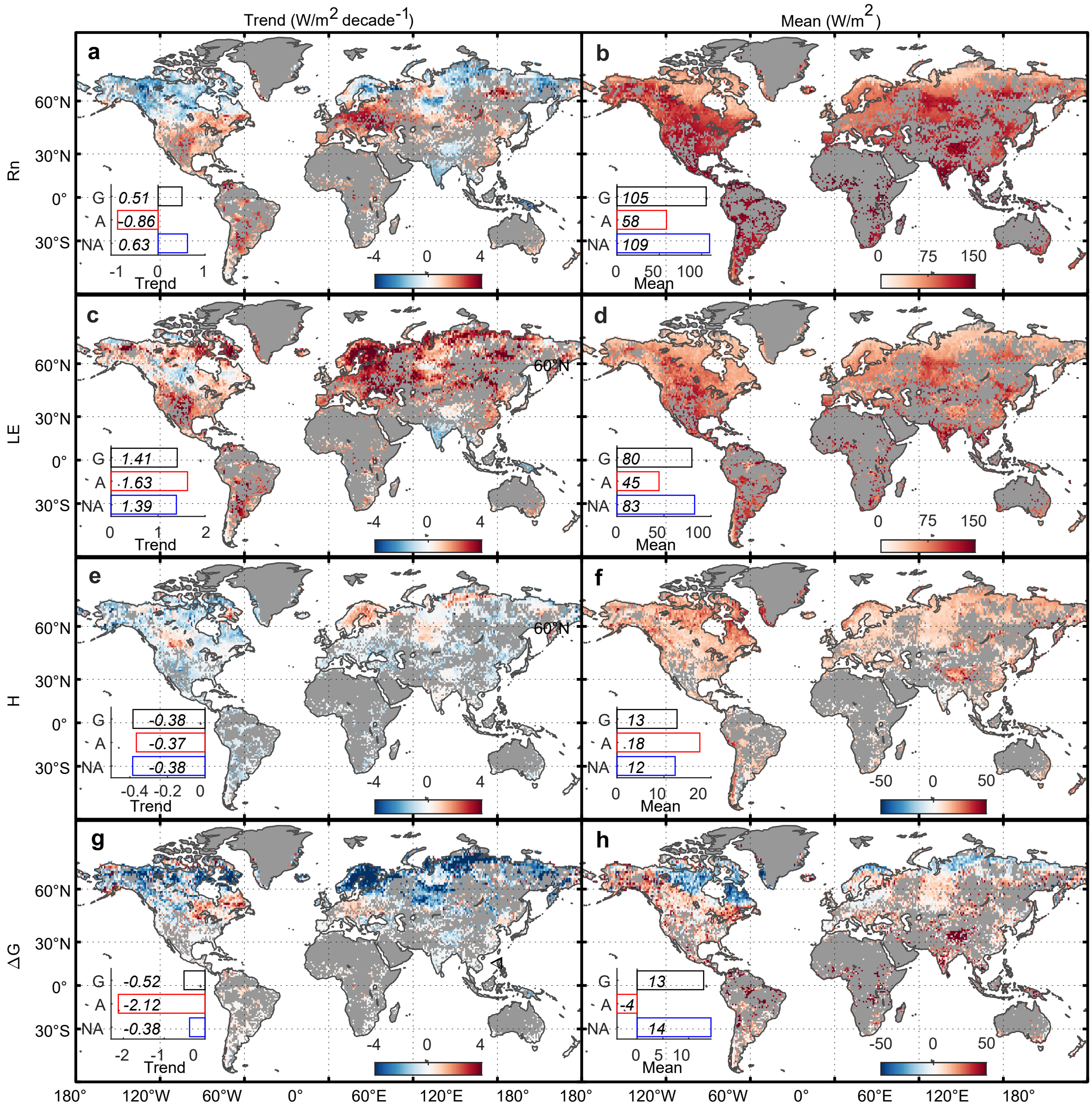
Trend (W/m2 decade-1)
Mean (W/m2)
a
b
c
d
e
f
g
h
Rn
LE
H
ΔG
60°N
30°N
0°
30°S
G
A
NA
0.51
-0.86
0.63
-1 0 1
Trend
105
58
109
0 50 100
Mean
1.41
1.63
1.39
0 1 2
Trend
80
45
83
0 50 100
Mean
-0.38
-0.37
-0.38
-0.4 -0.2 0
Trend
13
18
12
0 10 20
Mean
-0.52
-2.12
-0.38
-2 -1 0
Trend
13
-4
14
0 5 10
Mean
-4 0 4
0 75 150
-50 0 50
180° 120°W 60°W 0° 60°E 120°E 180°

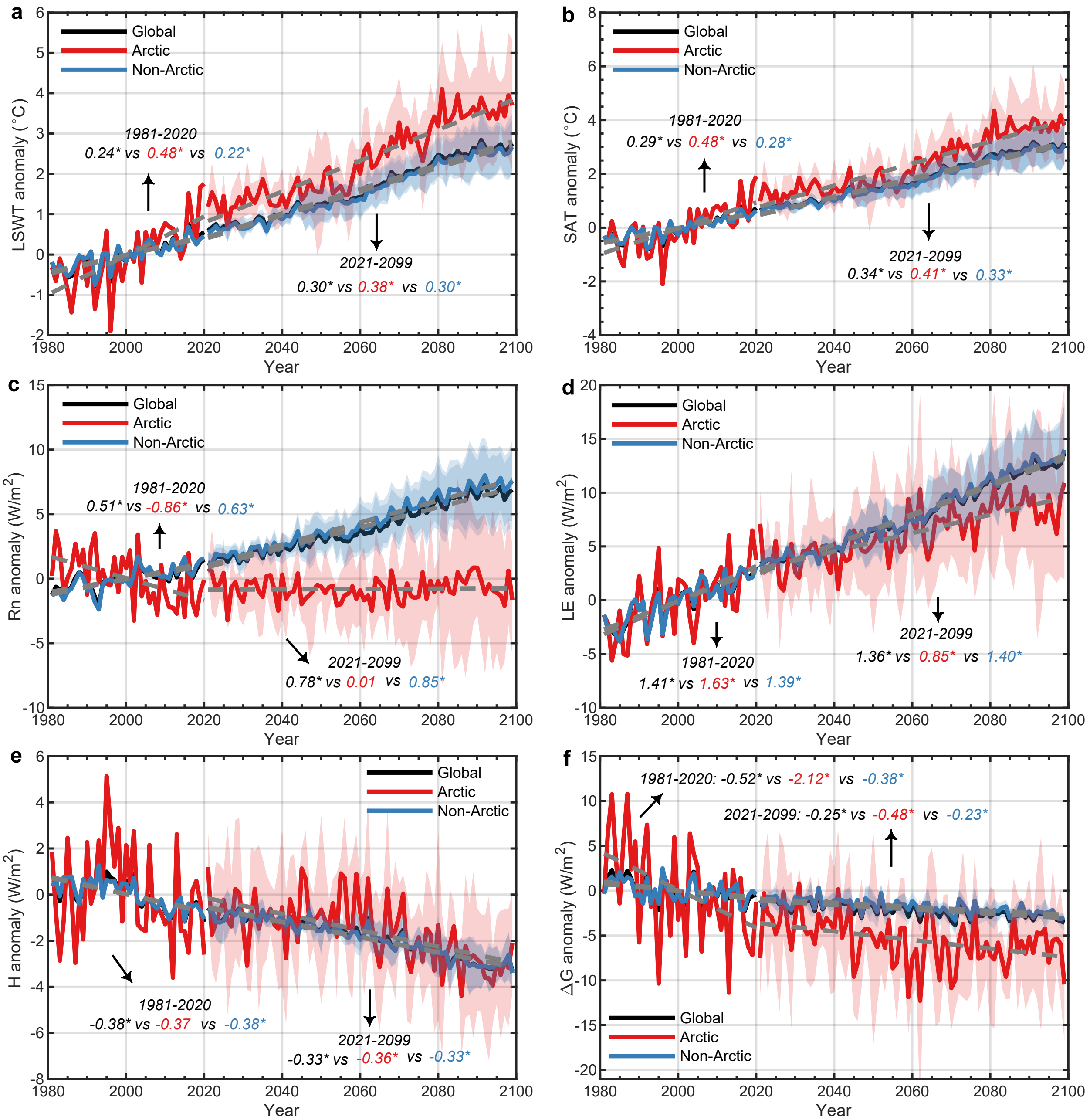
a
LSWT anomaly (°C)
Global
Arctic
Non-Arctic
1981-2020
0.24* vs 0.48* vs 0.22*
2021-2099
0.30* vs 0.38* vs 0.30*
Year
b
SAT anomaly (°C)
Global
Arctic
Non-Arctic
1981-2020
0.29* vs 0.48* vs 0.28*
2021-2099
0.34* vs 0.41* vs 0.33*
Year
c
Rn anomaly (W/m2)
Global
Arctic
Non-Arctic
1981-2020
0.51* vs -0.86* vs 0.63*
2021-2099
0.78* vs 0.01 vs 0.85*
Year
d
LE anomaly (W/m2)
Global
Arctic
Non-Arctic
1981-2020
1.41* vs 1.63* vs 1.39*
2021-2099
1.36* vs 0.85* vs 1.40*
Year
e
H anomaly (W/m2)
Global
Arctic
Non-Arctic
1981-2020
-0.38* vs -0.37 vs -0.38*
2021-2099
-0.33* vs -0.36* vs -0.33*
Year
f
ΔG anomaly (W/m2)
1981-2020: -0.52* vs -2.12* vs -0.38*
2021-2099: -0.25* vs -0.48* vs -0.23*
Global
Arctic
Non-Arctic
Year
1980
2000
2020
2040
2060
2080
2100